

## THE GEOMETRY AND IONIZATION STRUCTURE OF THE WIND IN THE ECLIPSING NOVA-LIKE VARIABLES RW TRI AND UX UMA

ULRICH M. NOEBAUER<sup>1,2</sup>, KNOX S. LONG<sup>1</sup>, STUART A. SIM<sup>2</sup>, AND CHRISTIAN KNIGGE<sup>3</sup>

*Accepted for publication in The Astrophysical Journal*

### ABSTRACT

The UV spectra of nova-like variables are dominated by emission from the accretion disk, modified by scattering in a wind emanating from the disk. Here, we model the spectra of RW Tri and UX UMa, the only two eclipsing nova-like which have been observed with the *Hubble Space Telescope* in the far-ultraviolet, in an attempt to constrain the geometry and the ionization structure of their winds. Using our Monte Carlo radiative transfer code, we computed spectra for simply parameterized axisymmetric biconical outflow models and were able to find plausible models for both systems. These reproduce the primary UV resonance lines – N V, Si IV, and C IV – in the observed spectra in and out of eclipse. The distribution of these ions in the wind models is similar in both cases as is the extent of the primary scattering regions in which these lines are formed. The inferred mass-loss rates are 6% – 8% of the mass accretion rates for the systems. We discuss the implication of our point models for our understanding of accretion disk winds in cataclysmic variables.

*Subject headings:* accretion, accretion disks — binaries: close — novae, cataclysmic variables — radiative transfer — stars: individual (RW Tri, UX UMa) — stars: winds, outflow

### 1. INTRODUCTION

Mass outflows are associated with accretion via a disk onto compact objects in a wide range of astrophysical systems, ranging from proto-stellar objects to close binaries and active galactic nuclei. The presence of mass outflow in all these systems, which cover a wide range of scales and system parameters, suggests an important connection between the processes of accretion and the outflow. Cataclysmic variables (CVs) are the closest astrophysical examples of such systems, and hence are an important test case for our understanding of outflows from disks. CVs are close binary systems consisting of a white dwarf (WD) and a low-mass late-type secondary star. The secondary overflows its Roche lobe, leading to mass transfer to the WD. Due to angular momentum conservation, the transferred material builds up an accretion disk around the WD (unless the magnetic field of the WD is large enough to disrupt the flow). Disk emission usually dominates other sources of light at visible wavelengths. Many CVs undergo outbursts of 3 – 5 mag lasting from days to weeks on timescales of weeks to years. The outbursts are due to a thermal instability in the disk which transforms the disk from a relatively cold, largely neutral gas to a hot, ionized plasma, increasing the accretion rate in the inner disk from about  $1 \times 10^{-11} M_{\odot} \text{ yr}^{-1}$  to  $10^{-9} - 10^{-8} M_{\odot} \text{ yr}^{-1}$  (Hōshi 1979; Mineshige & Osaki 1983). The frequency of outbursts depends on the longer term mass-transfer rate from the secondary, which for systems that undergo outbursts must be between the quiescent and outburst rate (Cannizzo 1993).

Far-ultraviolet (FUV) spectra of CVs obtained with the *International Ultraviolet Explorer* (*IUE*) were the first to show that CVs drive winds when the disk is in the high mass-transfer state (Krautter et al. 1981; Greenstein & Oke 1982; Córdoba & Mason 1982). Winds are not observed when CVs

are in the quiescent, low mass-transfer state. The signature of the wind is imprinted on the spectra in the form of P Cygni-like and/or blueshifted absorption profiles of resonance lines, such as N V, Si IV, and C IV. The blue edges of the absorption profiles imply velocities exceeding  $3000 \text{ km s}^{-1}$  in some systems (see, for a recent example, Hartley et al. 2002). The *IUE* observations were used to show that the emission features are generally weak or absent in systems viewed at low inclination and progressively more prominent at higher inclination (La Dous 1991). Time-resolved *IUE* observations also demonstrated that line shapes in eclipsing and nearly eclipsing systems vary systematically through secondary conjunction, showing not only that the emission lines had to arise from a region at least comparable in size to that of the secondary star but also that the outflowing material was likely rotating (Córdoba & Mason 1985; Drew & Verbunt 1988). While initial modeling of CV winds favored spherical geometry for simplicity (Drew & Verbunt 1985; Mauche & Raymond 1987), the observed characteristics of the resonance lines in CVs have over time led to a consensus picture of a biconical mass outflow originating from the inner disk.

Shlosman & Vitello (1993), hereafter SV93, were the first to develop a radiative transfer code based on the Sobolev approximation that was capable of determining the ionization structure of a biconical outflow emerging from the disk and of modeling C IV line profiles. They then used this to attempt to constrain the wind geometry of non-magnetic CVs. Vitello & Shlosman (1993) found that they could reproduce the observed profiles of C IV in three systems — RW Sex, RW Tri, and V Sge — with plausible geometries and mass-loss rates; they also found that they could produce similar C IV profiles with quite different accretion rates by changing other parameters in their kinematic description of the wind. Subsequently, Knigge, Wood & Drew (1995), hereafter KWD95, developed another Monte Carlo radiative transfer code which solved the radiative transfer exactly using a slightly different kinematic prescription for a biconical wind. Their code did not calculate the ionization balance in the outflow and instead

<sup>1</sup> Space Telescope Science Institute, 3700 San Martin Drive, Baltimore, MD 21218, USA

<sup>2</sup> Max Planck Institute for Astrophysics, Karl-Schwarzschild-Str. 1, 85748 Garching, Germany

<sup>3</sup> Department of Physics, University of Southampton, Southampton SO17 1BJ UK

assumed constant ionization fractions throughout. As had Shlosman & Vitello (1993), they were able to reproduce qualitatively many of the basic characteristics of C IV line profiles in disk-dominated CVs. Knigge & Drew (1997) applied their code to high-resolution time-resolved *Hubble Space Telescope* (*HST*) spectra of C IV of the eclipsing nova-like variable UX UMa, concluding that one not only needed a fast wind with a wide opening angle but a relatively dense, slow-moving transition region between the photosphere of the disk and the wind.

Despite the clear observational indications for the presence of mass outflow in CVs, much is still unknown about the physics of these winds, in particular the driving mechanisms. By analogy with O-star winds, most have assumed that the winds of CVs are radiatively driven. Hydrodynamical simulations seem to broadly support this picture (Proga et al. 2002), even though questions regarding whether CV disks are luminous enough to drive the required mass outflow remain (Drew & Proga 2000). Alternatives, magnetically driven or magnetically assisted flows from the disk or boundary layer region exist, based on suggestions that can be traced to, among others, Blandford & Payne (1982) and Pringle (1989), and are widely discussed for other disk systems, ranging from young stellar objects to active galactic nuclei (see, e.g., Königl et al. 2010; Campbell 2010). An important obstacle to a confident identification of the driving mechanism is that even basic wind parameters, such as the mass-loss rate, the acceleration, collimation, and ionization structure, remain poorly constrained. Thus obtaining reliable information on the wind structure, and especially about the ionization in the wind, should lead to a much better understanding of the physics underlying CV winds. In the long term, this might even allow us to gain insight into other types of accreting systems, as mass outflows seem to be a general feature of such systems.

Nova-like variables are disk-dominated CVs, which, unlike most other CVs, are nearly always observed in the “outburst” state. This is presumably because they have a higher mean mass-transfer rate than other types of CV (e.g., dwarf novae; Schreiber & Gänsicke 2002). Nova-like variables have orbital periods just above the period gap in non-magnetic CVs, where magnetic braking is thought to produce the largest mass-transfer rates in the long-term evolution of CVs (Howell et al. 2001). Because they stay in the high mass-transfer state for long periods of time, they may be the closest examples to steady-state accretion disks among the CVs. RW Tri and UX UMa are the two brightest eclipsing examples of this class. Eclipsing systems are of particular interest in the study of CVs, and, in particular, the winds of CVs, since time-resolved observations of the eclipse provide spatial information about the disk and wind properties that is unavailable for systems viewed at lower inclinations.

Here, we describe our efforts to model the *HST* spectra of RW Tri and UX UMa in an attempt to place constraints on the wind geometry and the ionization structure. These are the only eclipsing nova-like CVs for which medium spectral resolution, time-resolved UV spectra exist. The observations of RW Tri have been briefly discussed by Mason et al. (1997); the observations of UX UMa have been discussed more extensively by Mason et al. (1995), Mason et al. (1997), Knigge & Drew (1997), Baptista et al. (1998), Froning et al. (2003), and Linnell et al. (2008). With the partial exception of Knigge & Drew (1997), the earlier studies were primarily focused on modeling the accretion disk and WD in UX

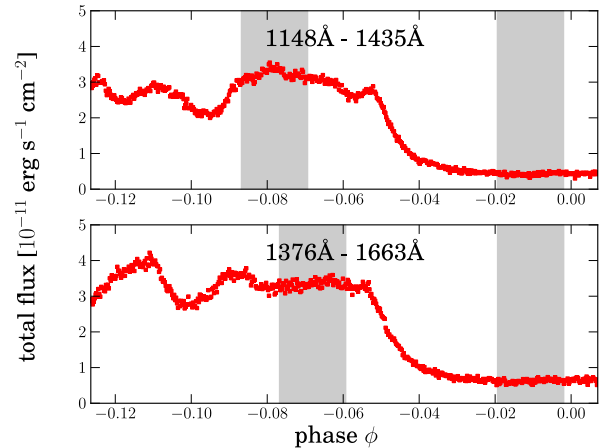


**Figure 1.** Light curves of the two RW Tri observations that were used to construct average pre-eclipse and mid-eclipse spectra. The phase of each measurement was derived with the revised ephemeris of RW Tri of Groot et al. (2004). The measurements in the upper panel all cover the shorter wavelength band from 1148 Å to 1425 Å, the observations in the lower panel were taken in the band from 1376 Å to 1663 Å. The phase intervals that were used for the averaging process are shaded in gray.

UMa. However, no one has attempted to constrain the properties of the wind in these systems by modeling all of the prominent wind lines simultaneously. The remainder of this paper is organized as follows. In Section 2, we describe the time-resolved observations of RW Tri and UX UMa with the Goddard High Resolution Spectrograph (GHRS) and the selection of the spectra we attempt to model. In Section 3, we describe briefly the radiative transfer code developed by Long & Knigge (2002) to produce synthetic spectra from parameterized models of biconical outflows, which we use to generate synthetic spectra. Then, in Section 4, we describe the strategy we used to identify models for the systems, and in Section 5, we discuss the degree to which we were able to reproduce the observe spectra and the implications of the results on the wind geometry of RW Tri and UX UMa. Finally, in Section 6, we summarize what we have learned through our attempt to model the pre-eclipse and eclipse spectra of RW Tri and UX UMa.

## 2. OBSERVATIONS

UV spectra of the nova-like RW Tri and UX UMa were obtained with the GHRS instrument on *HST* in late 1996 and early 1997 (as part of programs 6494 and 6024) and are described by Mason et al. (1997). Both systems were observed in order to explore time variations in the spectra as a function of the orbital phase. All of the observations discussed here were performed with the G140L grating, providing a wavelength resolution of 0.57 Å, in the rapid read-out mode, in which spectra were recorded at 5 s intervals. Each observation covers one of two overlapping wavelength intervals, each with a bandwidth of about 287 Å so that spectra from separate observations must be combined to yield the full spectral range from 1150 Å to 1660 Å. The observations of UX UMa and RW Tri each comprised about nine *HST* orbits. An observation log is presented in Table 1. To carry out this study, we retrieved and used the final reprocessed data from the *HST* archive.

To facilitate comparison of the synthetic spectra to the actual spectra of RW Tri and UX UMa, we averaged the ob-

**Table 1**  
Observation Log for *HST* Spectra of RW Tri and UX UMa.

ObsID	Obs. Start (MJD)	Spectral range (Å)	Phase Coverage
UX UMa			
z3fy0304t	50398.2014	1148-1435	0.654 - 0.701
z3fy0306t	50398.2132	1376-1663	0.714 - 0.762
z3fya102t *	50395.1085	1148-1435	-0.073 - 0.033
z3fya302t	50398.2554	1148-1435	-0.071 - 0.093
z3fya102t	50395.1751	1376-1663	0.027 - 0.377
z3fya104t	50395.1998	1148-1435	0.391 - 0.431
z3fya106t	50395.2422	1148-1435	0.607 - 0.647
z3fya108t	50395.2526	1376-1663	0.660 - 0.771
z3fya10at *	50395.3091	1376-1663	0.053 - 0.111
RW Tri			
z3kxa102t	50471.3006	1148-1435	0.395 - 0.433
z3kxa104t	50471.3446	1148-1435	0.585 - 0.718
z3kxa106t *	50471.4116	1148-1435	-0.126 - 0.007
z3kxa202t	50470.6978	1148-1435	0.796 - 0.893
z3kxa204t	50470.7418	1148-1435	-0.015 - 0.118
z3kxa302t	50474.3154	1148-1435	0.395 - 0.433
z3kxa304t	50474.3593	1376-1663	0.585 - 0.718
z3kxa306t *	50474.4263	1376-1663	-0.126 - 0.007
z3kxa402t	50473.7126	1376-1663	0.796 - 0.833
z3kxa404t	50473.7566	1376-1663	-0.015 - 0.118
z3kxb102t	50471.4786	1376-1663	0.162 - 0.296
z3kxb302t	50474.4933	1376-1663	0.163 - 0.296

**Note.** Average spectra are constructed from observations labeled with an asterisk (\*).

served spectra over specific phase intervals. There were certain difficulties associated with this. At any time observations only covered parts of the spectral range of interest and the phase coverage was also not ideal for either UX UMa or RW Tri, as indicated in Table 1. For RW Tri, two observations sampled pre-eclipse and mid-eclipse orbital phase. The other observations covered only parts of the mid-eclipse and the post-eclipse state. In both cases, one observation existed for each wavelength band. For UX UMa, there was only one observation covering the eclipse in the 1375 – 1665 Å band, but two covering the shorter wavelength band from 1148 Å to 1435 Å. To construct representative spectra for the mid-eclipse and the pre-eclipse phase, both RW Tri observations containing information of these two states were taken. For UX UMa, the two observations in the 1148 – 1435 Å band had different overall pre-eclipse flux levels but showed no striking differences in spectral shape. Therefore, only the observation which was closest to the overall flux level of the only measurement set in the longer wavelength band was used. The spectra used in our study were obtained by averaging over representative phase intervals. Choosing the width and the position of these intervals was, at least in the pre-eclipse case, somewhat arbitrary, but tests showed that the overall flux level and the spectral features in the average spectra were not very sensitive to these choices. In the end, we used the highlighted regions in Figures 1 and 2 for the averaging process. The resulting spectra were finally merged to cover the entire wavelength band from 1148 Å to 1665 Å by averaging over the overlapping region. Figures 3 and 4 show the resulting pre-eclipse and eclipse spectra for UX UMa and RW Tri, respectively. According to Rutten et al. (1992), RW Tri is thought to lie along a line of sight with  $E(B-V)$  of 0.1, and so to facilitate comparisons with models the spectra for RW Tri were corrected for reddening. Reddening along the line of sight to UX

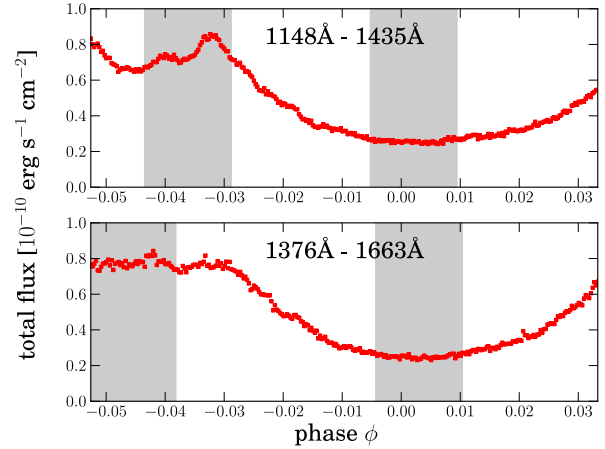


**Figure 2.** Light curves of UX UMa. The phase of each measurement was determined with the ephemeris of UX UMa derived by Baptista et al. (1995). The upper panel shows the observation in the short wavelength band. In the lower panel, the observation covering the long wavelength band is displayed. The average spectra were constructed from the shaded regions.

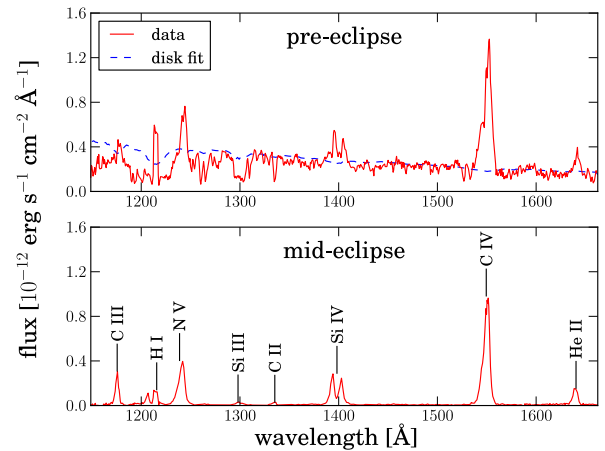


**Figure 3.** Average RW Tri *HST* pre-eclipse and mid-eclipse spectra obtained by averaging over the regions highlighted in Figure 1. In the pre-eclipse panel, the result of fitting the continuum to an accretion disk radiating as an ensemble of stellar atmospheres is also shown. The main emission lines are shown in the lower panel.

UMa is believed small ( $E(B-V) < 0.04$ , Verbunt 1987), so no correction was made for UX UMa.

The pre-eclipse spectra of both RW Tri and UX UMa show rather flat continua with a number of superimposed resonance lines. During eclipse the continuum is suppressed and the spectrum is dominated by the emission lines that, because the disk is eclipsed, must arise from an extended region.

The three major resonance lines present in both systems are the doublets N V  $\lambda\lambda 1239, 1243$ , Si IV  $\lambda\lambda 1394, 1403$ , and C IV  $\lambda\lambda 1548, 1551$ . Apart from these there are additional, weaker lines of low-ionization state metals such as C II  $\lambda 1333$ , C III  $\lambda 1176$ , and Si III  $\lambda\lambda 1295 - 1303$  and lines of both hydrogen (H I Lyman  $\alpha$   $\lambda 1215$ ) and helium (He II  $\lambda 1640$ ) are visible. In the pre-eclipse state of both systems, the low ionization state lines, especially those of C II  $\lambda 1333$  and Si III  $\lambda\lambda 1295 - 1303$  are seen as deep absorption dips,

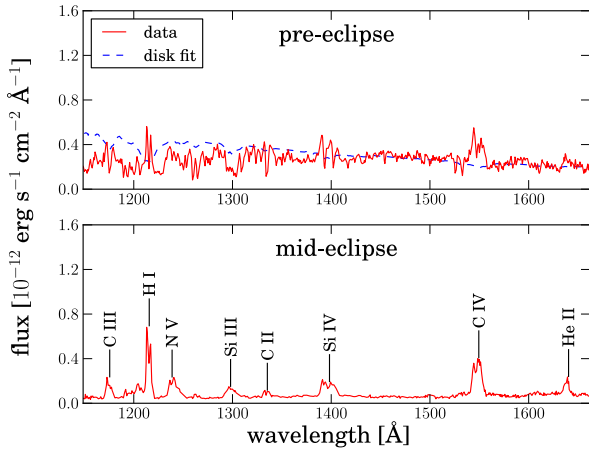


**Figure 4.** Average UX UMa *HST* pre-eclipse and mid-eclipse spectra. Again emission lines are identified in the lower panel and the disk continuum fit is shown in the upper panel.

suggesting that the main concentration of these ions lies in the line of sight. The UX UMa pre-eclipse spectra generally show many absorption features, including in the main resonance lines: for example, two prominent narrow dips are present in the Si IV line and one in the C IV line.

### 3. RADIATIVE TRANSFER CODE AND WIND MODELS

In order to place limits on the geometry of the winds in RW Tri and UX UMa using the spectra, we need to model the effect of the wind on the spectra. Our working hypothesis is that the winds arise in a biconical outflow. To model the spectra we parameterize the outflow using one of two kinematic descriptions for the wind and we use a Monte Carlo radiative transfer code (PYTHON, developed by Long & Knigge 2002, with improvements described by Sim et al. 2005) to calculate the ionization structure of the wind and to create synthetic spectra. The chemical composition of the wind material is fixed to the solar abundances determined by Anders & Grevesse (1989). Here, we give a short summary of the important features of this program and the two classes of parameterized wind models which we use in this study (for full details, see Long & Knigge 2002).

#### 3.1. Monte Carlo approach

PYTHON operates by performing a sequence of Monte Carlo simulations in which the quanta are packets of radiative energy. These packets are launched in accordance with the specified radiation sources (see below) and propagate through a parameterized model for the CV disk wind. As the packets propagate, they can interact with the wind material via electron scattering, resonance line scattering, bound-free absorption, or free-free absorption. Their trajectories are finally terminated when they either escape, lose all their energy to absorption in the wind, or are lost from the simulation by striking the WD, disk surface, or companion star.

Since the ionization and heating of the wind are controlled by the radiation, the ionization and thermal state must be computed self-consistently with the local radiation field properties. This is achieved via an iteration sequence. In each iteration, the wind properties are held fixed while a Monte Carlo simulation of the radiation field is performed. During the Monte Carlo simulation, estimators for the local radiation

field properties (radiation temperature  $T_R$  and dilution factor  $W$ ) are recorded for each grid cell in the wind and used to make an improved estimate of the wind ionization state and kinetic temperature  $T_e$  for use in the next iteration.

Once the wind properties reach convergence, a final sequence of additional Monte Carlo simulations for the converged wind properties are used to obtain the observed spectrum for the desired inclination angle. In these final simulations, a modified version of the technique described by Woods (1991) is used: in every interaction with the wind medium the packet contributes to the final spectrum according to the probability of emission into the observer’s line of sight after the interaction.

#### 3.1.1. Radiation sources

The calculations presented in this work include radiation by the WD and its accretion disk. The disk is the primary source of radiation in non-magnetic CVs in the high mass-transfer state. It is treated as a geometrically thin but optically thick disk which follows the standard temperature distribution (e.g., Wade 1984)

$$T_{\text{eff}} = \left( \frac{3GM_{\text{acc}}M_{\text{WD}}}{8\pi\sigma R_{\text{WD}}^3} \right)^{1/4} \left( \frac{R_{\text{WD}}}{R} \right)^{3/4} \left( 1 - \sqrt{\frac{R_{\text{WD}}}{R}} \right)^{1/4}. \quad (1)$$

The disk radiation is composed from an ensemble of 300 concentric annuli each of which radiates a spectrum at the local value of  $T_{\text{eff}}$ . The inner and outer boundaries of each annulus are determined by the requirement that all annuli should emit an equal fraction of the total disk luminosity. For this study, we model the spectrum from each disk annulus as a black body during the iteration processes used to obtain the ionization state. In the spectrum calculation, the disk emission is described by synthetic stellar spectra created with TLUSTY/SYNSEX (Hubeny & Lanz 1995). When synthetic spectra are used, the calculation of the effective gravity of the disk follows the prescription given by Herter et al. (1979). To describe the WD radiation, a single black body/Hubeny model is used. The secondary star is treated as a dark absorber.

The PYTHON code can also account for radiation from a boundary layer parameterized by a luminosity and temperature as described by Long & Knigge (2002). We found, however, that if we included a hot luminous boundary layer (such as introduced by Knigge & Drew 1997) the wind was typically too highly ionized to obtain a good match with observed spectra. We therefore opted to exclude any such boundary layer from the calculations. This may imply that either the WD has significant rotation or that the boundary layer geometry is such that much of the wind is not exposed to its radiation.

The energy emitted by the radiation sources is discretized into energy packets, each with its own direction of propagation, frequency, and weight. The packets are initialized with weights corresponding to the fraction of the physical luminosity carried by the package and frequency sampled randomly from the luminosity spectra of the WD and accretion disk annuli. Initial directions of propagation are assigned assuming a linear limb-darkening law and initial positions are located on either the WD or disk surface, as appropriate. In addition to the primary radiation sources, the code also accounts for free-free, free-bound, and bound-bound emission by the

wind, based on its local ionization state and kinetic temperature.

### 3.1.2. Wind conditions

A key component of modeling the wind spectrum is a realistic treatment of the wind ionization state. In contrast to some previous studies in which uniform ionization conditions throughout the wind were assumed (e.g., Knigge, Wood & Drew 1995), PYTHON computes the ionization state as a function of position using the modified nebular approximation described by Mazzali & Lucy (1993)

$$\frac{n_{j+1}n_e}{n_j} = W[\xi + W(1 - \xi)] \left(\frac{T_e}{T_R}\right)^{1/2} \left(\frac{n_{j+1}n_e}{n_j}\right)^* . \quad (2)$$

Here,  $W$  is a dilution factor,  $\xi$  is the fraction of recombinations that go directly to the ground state, and  $T_e$  and  $T_R$  are the electron and radiation temperatures, respectively. The asterisk denotes quantities to be evaluated in local thermodynamic equilibrium at  $T_R$ .

In contrast to Mazzali & Lucy (1993), however, we do not assume a simple relationship between  $T_R$  and  $T_e$  but instead calculate  $T_e$  independently from the assumption of thermal equilibrium (i.e., the heating and cooling rates are in equilibrium at every point in the wind). As noted above,  $T_R$ ,  $W$ , and  $T_e$  are not known a priori, but are determined by an iterative sequence of Monte Carlo experiments. In practice,  $T_R$  is the most important parameter for the ionization balance (given by Equation (2)) and is primarily determined by the temperature distribution in the disk. This in turn depends on the adopted system parameters (WD mass and radius, and the mass accretion rate  $\dot{M}$ ).

### 3.2. Wind models

For our simulations, we adopt two classes of simply parameterized wind models, those developed by SV93 and KWD95. We carried out our studies using both wind models so that we could investigate any sensitivity of our results to the parameterization. As demonstrated below, however, we find that our conclusions are relatively insensitive to this choice. Both of these models describe the wind as a stationary biconical outflow emerging from both sides of the accretion disk. In each case, the velocity in the wind consists of a rotational component  $v_\phi$  and a poloidal component  $v_q$ . The rotational component is obtained assuming that the wind streamlines rise from a disk in Keplerian rotation and that specific angular momentum is conserved as the flow moves outward:

$$v_\phi(r)r = v_{(\phi,0)}(R)R , \quad (3)$$

$$v_{(\phi,0)}(R) = \sqrt{\frac{GM_{\text{WD}}}{R}} . \quad (4)$$

Here, and in the following,  $r$  stands for the radial position of a point in the wind, while  $R$  denotes the radius at which the wind streamline passing through the point reaches the accretion disk. The poloidal velocity field in the wind causes material to spiral on streamline cones away from the disk. The detailed geometry of these cones depends on which of the wind prescriptions is used. This, together with the way of parameterizing the poloidal velocity and calculating the wind density, is the main difference between the two classes of wind models we consider.

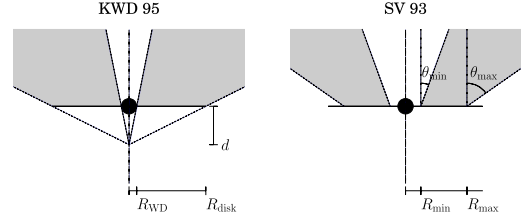


**Figure 5.** Left: wind geometry as parameterized by KWD95. The black circle denotes the WD and the horizontal line the accretion disk. Note that the wind shape is controlled by only one collimation parameter,  $d$ , which is usually given in units of  $R_{\text{WD}}$ . Right: wind geometry as parameterized by SV93. In both panels, the mass outflow region is shaded in gray. For illustrative purposes only one half of the wind structure is shown (the wind is symmetric under reflection in the  $xy$ -plane).

#### 3.2.1. KWD95 wind model

KWD95 parameterize the wind as a biconical outflow from the entire accretion disk and characterize its geometry by only one parameter  $d$ . By definition, this parameter specifies the position of a point on the rotational axis where extrapolations of all streamline cones meet. Together with the disk extent  $[R_{\text{WD}}, R_{\text{disk}}]$ ,  $d$  defines the opening angles of the wind. Figure 5 illustrates the wind geometry of the KWD95 treatment.

The wind region itself is characterized by a density and a velocity. The density in the wind is specified by the mass-loss rate per area in the disk. This quantity is assumed to follow the temperature distribution in the disk

$$\dot{m}(R) = \dot{M}_{\text{wind}} \frac{T_{\text{eff}}^{4\alpha}(R)}{\int dA' T_{\text{eff}}^{4\alpha}(R')} . \quad (5)$$

The integral in the denominator ensures the normalization to the total mass-loss rate  $\dot{M}_{\text{wind}}$  when integrated over the disk surface from which the wind emerges. The exponent  $\alpha$  allows the mass-loss rate per unit area to be tied to the local disk effective temperature ( $\alpha = 0.25$ ) or the luminosity ( $\alpha = 1.0$ ) in the disk. The mass-loss rate per area can be used together with the poloidal velocity  $v_{(q,0)}$  at the streamline base and the polar angle of the streamline  $\delta = \arctan \frac{R}{d}$  to calculate the density at the base of the streamline

$$\rho_0(R) = \frac{\dot{m}(R)}{v_{(q,0)}(R) \cos \delta} . \quad (6)$$

As the wind rises from the disk, the density decreases as

$$\rho(r) = \rho_0(R) \left(\frac{d}{q \cos \delta}\right)^2 \frac{v_{(q,0)}(R)}{v_q(r)} . \quad (7)$$

Here  $q$  denotes the distance to the point  $d$  on the rotational axis. The poloidal velocity component  $v_q(r)$  depends on three parameters, the acceleration length  $R_s$ , acceleration exponent  $\beta$ , and terminal velocity  $v_\infty$ :

$$v_q(l) = c_s(R) + [v_\infty - c_s(R)] \left(1 - \frac{R_s}{R_s + l}\right)^\beta . \quad (8)$$

The terminal velocity is parameterized as a multiple ( $f$ ) of the local escape speed

$$v_\infty = f v_{\text{esc}} = f \sqrt{\frac{2GM_{\text{WD}}}{R}} \quad (9)$$

and the poloidal velocity is assumed to be equal to the local sound speed at the base of the wind streamlines.

$$c_s(R) = 10 \cdot \sqrt{\frac{T_{\text{eff}}(R)}{10^4}} \text{ km s}^{-1}. \quad (10)$$

The quantity  $l$  in Equation (8) represents the distance of the point  $r$  to the accretion disk, measured on the streamline cone.

In total there are six parameters,  $d$ ,  $\alpha$ ,  $\beta$ ,  $\dot{M}_{\text{wind}}$ ,  $f$ , and  $R_s$  which specify the CV wind in the KWD95 parameterization. Although the true geometry is controlled only by  $d$ , the extent of the wind region in which the ion concentrations are sufficiently high to lead to strong spectral lines is strongly sensitive to the distribution of mass outflow from the disk, as determined by  $\dot{M}_{\text{wind}}$  and  $\alpha$ . In particular, high values of the exponent  $\alpha$  will cause a very high density near the rotational center of the wind and a very dilute outflow at the outer edges of the wind while decreasing  $\alpha$  moves more material to the outer edges. Thus, the effective collimation is determined by a combination of  $d$  and  $\alpha$ .

### 3.2.2. SV93 wind model

SV93 presented a wind model that is more flexible than the KWD95 treatment, but involves more free parameters. In the SV93 description, the wind does not necessarily emerge from all parts of the disk. Instead, the wind region is specified by a minimum and a maximum disk radius  $R_{\text{min}}$  and  $R_{\text{max}}$ . Similarly, the collimation of the wind is specified by a minimum and a maximum streamline angle  $\theta_{\text{min}}$  and  $\theta_{\text{max}}$ . Figure 5 illustrates the wind geometry in the SV93 model. The distribution of streamline angles throughout the disk is determined by an additional parameter  $\gamma$  defined via

$$\theta(R) = \theta_{\text{max}} + (\theta_{\text{max}} - \theta_{\text{min}})x(R)^\gamma, \quad (11)$$

where

$$x(R) = \frac{R - R_{\text{min}}}{R_{\text{max}} - R_{\text{min}}}. \quad (12)$$

As in the KWD95 description,  $R$  is the radius of the point at which the streamline passing through point  $r$  crosses the disk plane.

The rotational velocity in the SV93 wind model is exactly the same as in the KWD95 description (see Equations (3) and (4)). The poloidal velocity ( $v_q$ ) at a distance  $l$  measured on the streamline cone is specified in terms of three parameters: an acceleration length scale  $R_s$ , acceleration exponent  $\alpha$ , and the terminal velocity  $v_\infty$

$$v_q(l) = v_0 + (v_\infty - v_0) \left[ \frac{(l/R_s)^\alpha}{(l/R_s)^\alpha + 1} \right]. \quad (13)$$

We follow SV93 in adopting  $v_0 = 6 \text{ km s}^{-1}$ . As in the KWD95 prescription, the terminal velocity is specified in units of the local escape speed (see Equation (9)).

Again, the wind density is determined by the disk mass-loss rate per unit area  $\dot{m}$ . In the SV93 prescription, this is not specified in terms of the local disk temperature but is assumed to follow the relation

$$\dot{m}(R) = \dot{M}_{\text{wind}} \frac{R^\lambda \cos \theta(R)}{\int dA' R'^\lambda \cos \theta(R')}. \quad (14)$$

The normalization ensures that calculating the total mass-loss rate is given by  $\dot{M}_{\text{wind}}$  while  $\lambda$  allows for variation in the mass loading of wind streamlines. The density in the wind is then given by

$$\rho(r, z) = \frac{R}{r} \frac{dR}{dr} \frac{\dot{m}(R)}{v_z(r, z)}. \quad (15)$$

The  $R/r \, dR/dr$  factor results from the increasing area between streamlines the further the wind is away from the disk which, in the special case of streamlines on a cone with angle  $\theta$ , simplifies to

$$\frac{dr}{dR} = 1 + \frac{l(d\theta/dR)}{\cos \theta}. \quad (16)$$

As in the KWD95 description,  $l$  is the distance to the disk on the streamline cone.

In total, the SV93 prescription requires ten parameters to define the wind:  $\gamma$ ,  $R_{\text{min}}$ ,  $R_{\text{max}}$ ,  $\theta_{\text{min}}$ ,  $\theta_{\text{max}}$ ,  $\lambda$ ,  $R_s$ ,  $\alpha$ ,  $f$ , and  $\dot{M}_{\text{wind}}$ . The collimation of the wind is primarily determined by  $\theta_{\text{min}}$  and  $\theta_{\text{max}}$ , supplemented by the effects of  $\lambda$ .

## 4. FINDING FIDUCIAL MODELS: BASIC APPROACH

Our primary objective is to constrain the physical properties of the wind. The empirical wind models described in the previous section involve a rather large number of parameters, too many for it to be computationally practical to compute large grids of model spectra that explore the complete parameter space. Therefore, we have chosen to accept previous determinations of the system parameters, where possible, and focus our study on the major parameters of the wind itself.

The distance to RW Tri has been determined to be  $D = 341_{-31}^{+38}$  pc from its parallax (McArthur et al. 1999). This is almost identical to the distance obtained by Rutten et al. (1992) from the analysis of the optical eclipse light curve. According to Rutten et al. (1992) the WD mass for RW Tri is about  $0.7 M_\odot$ , which is typical of WDs in other systems and the mass ratio is fairly close to 1. In their study they also estimate that the inclination for RW Tri is about  $75^\circ$ , although this is somewhat uncertain and values as low as  $67^\circ$  (Kaitchuck et al. 1983) and as high as  $80^\circ$  (Mason et al. 1997) have been suggested. From spectroscopic studies, Kaitchuck et al. (1983) also determined the  $K$  velocity of the WD. The amplitude of this velocity is roughly  $200 \text{ km s}^{-1}$ . Table 2 lists the system parameters we adopted for RW Tri.

The main source for the continuum flux in nova-like variables is normally the accretion disk. For a given wind model, the ionization structure is primarily determined by the radiation temperature  $T_R$ , which, for a steady state, is controlled by the effective temperature ( $T_{\text{eff}}$ ) of the disk. Assuming that the disk radiates as an ensemble of stellar atmospheres, as described by Equation (1), then the mass accretion rate is a function of the observed flux, the distance, inclination, and the mass and radius of the WD. Thus, we can use the observed continuum flux and system parameters to constrain the mass accretion rate and avoid treating it as a completely free parameter in our studies. For this exercise, we restricted the wavelength range for the continuum fits to the regions between the Si IV, C IV, and He II lines which show a

**Table 2**  
System Parameters for RW Tri and UX UMa.

System	Parameter	Value	Reference
RW Tri	$M_{\text{WD}}$	$0.7 M_{\odot}$	Rutten et al. (1992)
	$M_2$	$0.6 M_{\odot}$	Rutten et al. (1992)
	$i$	$75^{\circ}$	Rutten et al. (1992)
	$D$	330 pc	Rutten et al. (1992)
	$\dot{M}_{\text{acc}}$	$\sim 10^{-8.0} M_{\odot} \text{ yr}^{-1}$	Rutten et al. (1992)
	$K_1$	$\sim 200 \text{ km s}^{-1}$	Kaitchuck et al. (1983)
UX UMa	$M_{\text{WD}}$	$0.47 \pm 0.07 M_{\odot}$	Baptista et al. (1995)
		$0.78 \pm 0.13 M_{\odot}$	Vande Putte et al. (2003)
	$M_2$	$0.47 \pm 0.10 M_{\odot}$	Baptista et al. (1995)
		$0.47 \pm 0.07 M_{\odot}$	Vande Putte et al. (2003)
	$i$	$71.0 \pm 0.6^{\circ}$	Baptista et al. (1995)
	$D$	$345 \pm 34 \text{ pc}$	Baptista et al. (1995)
	$\dot{M}_{\text{acc}}$	$10^{-8.0 \pm 0.2} M_{\odot} \text{ yr}^{-1}$	Baptista et al. (1995)
	$K_1$	$\sim 200 \text{ km s}^{-1}$	Schlegel et al. (1983)

clean continuum in the observations (in contrast to the complex FUV region). For RW Tri, the continuum fits resulted in an accretion rate of  $8.3 \times 10^{-9} M_{\odot} \text{ yr}^{-1}$  (see Figure 3). Accounting for the uncertainties in the inclination ( $75_{-8}^{+5} \text{ }^{\circ}$ ), the distance ( $341_{-31}^{+38} \text{ pc}$ ) and the WD mass (here, an uncertainty of one-tenth of the solar mass was assumed), the valid range for the accretion rate would be  $2.7 \times 10^{-9} M_{\odot} \text{ yr}^{-1}$  to  $2.6 \times 10^{-8} M_{\odot} \text{ yr}^{-1}$ , corresponding to a maximum effective temperature of the disk between  $T_{\text{eff}} = 4.9 \times 10^4 \text{ K}$  and  $6.9 \times 10^4 \text{ K}$ .

The most determined effort to establish the system parameters for UX UMa was made by Baptista et al. (1995). They used a (different) set of high time resolution, low spectral resolution *HST* spectra, and modeled the time-dependent contribution of the disk and WD to the continuum to identify the phases associated with the eclipse of the WD. From this, they inferred a WD mass of  $0.47 \pm 0.07 M_{\odot}$ , and a mass ratio ( $M_2/M_{\text{WD}}$ ) of  $1 \pm 0.1$  and an inclination of  $71 \pm 1^{\circ}$ . They then derived a distance of  $345 \pm 34 \text{ pc}$  from eclipse maps of the system obtained from the combination of UV and *R*-band light curves. Since then, most workers, including most recently Linnell et al. (2008), have adopted these parameters for UX UMa. There are various reasons to question the accuracy of the measurements. First, if correct, the WD mass in UX UMa is much lower than that of most WDs (including most WDs in CV systems), and the mass ratio is at the limit allowed by conservative mass transfer. Second, at the temperature determined by Baptista et al. (1995) for the WD, the WD should have been evident in the *FUSE* spectra of UX UMa, but Froning et al. (2003), analyzing time-resolved *FUSE* observations of UX UMa, were unable to identify the WD ingress and egress in the light curve. Despite these concerns, we too adopt the parameters of Baptista et al. (1995), since no alternative values have been proposed with greater credibility. They are also listed in Table 2. The value for the  $K$  velocity of UX UMa, again  $\sim 200 \text{ km s}^{-1}$  was adopted from Schlegel et al. (1983).

According to the continuum fit (see Figure 4), the accretion rate for UX UMa is a little higher than RW Tri. It was determined as  $1.2 \times 10^{-8} M_{\odot} \text{ yr}^{-1}$  but values within the range of  $6.9 \times 10^{-9} M_{\odot} \text{ yr}^{-1}$  to  $1.9 \times 10^{-8} M_{\odot} \text{ yr}^{-1}$  would still be consistent with the system parameters considering the uncertainties in the WD mass, the inclination, and distance. This corresponds to a maximum disk effective temperature range of  $T_{\text{eff}} = 4.6 \times 10^4 \text{ K}$  to  $4.9 \times 10^4 \text{ K}$ .

In order to study the wind geometry and the ionization

structure of the mass outflow in UX UMa and RW Tri, we used PYTHON to develop “point” models for both systems. To avoid the computationally demanding brute-force method of computing grids of models and searching for the best-match spectrum, we adopted a hierarchical approach to searching the wind parameters. Our basic methodology was to come as close as possible to the observations by adjusting the overall ionization structure in the wind first. For that we started with the KWD95 descriptions and the wind parameters derived by Knigge & Drew (1997), applied to both our subjects of study, RW Tri and UX UMa, and explored different values of the mass accretion and the mass-loss rate — these are the primary parameters that determine the ionization conditions. However, we restricted the mass accretion rate to the values compatible with the results of disk continuum fits (see above). After exploring the  $\dot{M}_{\text{wind}} \times \dot{M}_{\text{acc}}$  parameter space, the influence of each of the remaining free wind parameters on the spectrum was tested, allowing us to successively obtain closer agreement with the observations. When using SV93 point models, the same approach was used except that the  $\dot{M}_{\text{wind}} \times \dot{M}_{\text{acc}}$  space was not re-explored and wind parameters which roughly correspond to the best KWD95 model were used as a starting point. With this approach we were able to explore the sensitivity of the spectrum to the main parameters although it did not lead to an exhaustive investigation of the complete parameter space. In general, determining our “best” models involved subjective criteria since perfect matches were never obtained. In these choices, we prioritized the overall strength and shape of the major emission lines.

Applying these strategies, we were able to find good point models for both systems using both wind treatments, SV93 and KWD95. The following sections are dedicated to presenting these models (both their successes and failures) and the conclusions drawn from them. Throughout our discussion, we focus on the three prominent emission lines of N V, Si IV, and C IV. As we shall show, these lines form across a wide range of conditions in the wind and, together, probe a significant fraction of the outflowing material. In addition, as resonance lines in Li- and Na-like ions, they involve relatively simple atomic physics which should be well described by our radiative transfer simulations. We will, however, also comment on other spectroscopic features formed by lower ionization state metal ions (which exist predominantly in the coolest/densest parts of the models) and recombination line features of both H and He.

## 5. RESULTS

We now present our point models for both RW Tri and UX UMa (see below) and then discuss the similarities and differences we infer for the wind structures in these systems.

Since we allowed for some flexibility in the mass accretion rate for a given set of system parameters, we have also allowed some freedom in the distance we adopt for both objects. Specifically, we always renormalized the model spectra to the observations in the discussion below. For this renormalization the continua of model and data were compared between Si IV and C IV. However, the implied deviations from the distances given in Table 2 are well within the uncertainties since the point models for both systems have accretion rates very close to the values determined by our disk continuum fits. We also corrected all pre-eclipse model spectra for the  $K$  velocity (redshift) of the WD. This shift however was rather small — from  $0.3 \text{ \AA}$  at the blue end to  $0.6 \text{ \AA}$  at the red end of the

**Table 3**  
Parameters for Our Best KWD95 Model for RW Tri and UX UMa.

Parameter	RW Tri		UX UMa
	Point Model	Point Model	KD 97 <sup>a</sup>
$M_{\text{WD}}$	$0.7 M_{\odot}$	$0.47 M_{\odot}$	
$M_2$	$0.6 M_{\odot}$	$0.47 M_{\odot}$	
$R_{\text{WD}}$	$8.0 \times 10^8 \text{ cm}$	$9.7 \times 10^8 \text{ cm}$	
$R_{\text{disk}}$	$2.4 \times 10^{10} \text{ cm}$	$2.9 \times 10^{10} \text{ cm}$	
$i$	$75^{\circ}$	$71^{\circ}$	
$D$ <sup>b</sup>	349 pc	374 pc	
$\dot{M}_{\text{disk}}$	$8.0 \times 10^{-9} M_{\odot} \text{ yr}^{-1}$	$1.3 \times 10^{-8} M_{\odot} \text{ yr}^{-1}$	$2.7 \times 10^{-8} M_{\odot} \text{ yr}^{-1}$
$T_{\text{eff}}$ <sup>c</sup>	$5.7 \times 10^4 \text{ K}$	$5.1 \times 10^4 \text{ K}$	
$\dot{M}_{\text{wind}}$	$4.8 \times 10^{-10} M_{\odot} \text{ yr}^{-1}$	$1.0 \times 10^{-9} M_{\odot} \text{ yr}^{-1}$	$1.0 \times 10^{-9} M_{\odot} \text{ yr}^{-1}$
$d$	20	35	15
$\alpha$	0.1	0.5	0.5
$f$	3.0	3.0	3.0
$R_s$	$4.0 \times 10^{10} \text{ cm}$	$4.9 \times 10^{10} \text{ cm}$	$4.9 \times 10^{10} \text{ cm}$
$\beta$	4.5	1.0	4.5

**Notes.**

<sup>a</sup> System and wind parameters from Knigge & Drew (1997). These parameters were used as a starting point when deriving our point models.

<sup>b</sup> Distance implied by the renormalization of the model continuum.

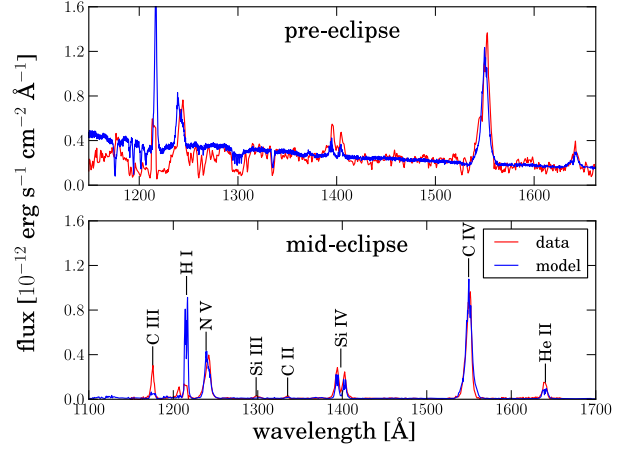
<sup>c</sup> Maximum effective temperature in the disk determined via Equation (1) from  $M_{\text{WD}}$ ,  $R_{\text{WD}}$ ,  $\dot{M}_{\text{disk}}$ .

spectrum.

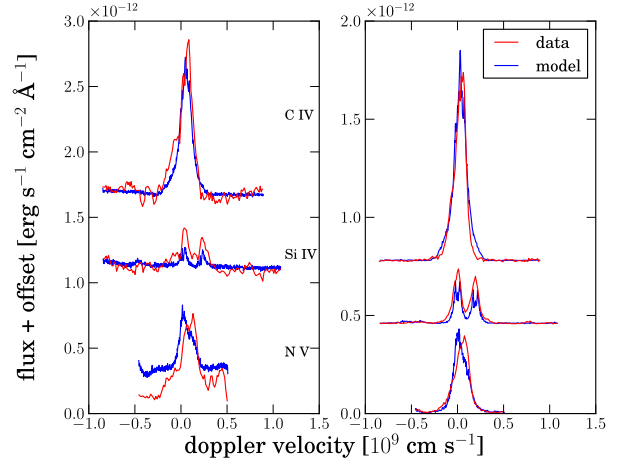
### 5.1. RW Tri

Table 3 gives the parameters of our best model for RW Tri obtained with the KWD95 wind description via our strategy described in Section 4. Exploration of the  $\dot{M}_{\text{wind}} \times \dot{M}_{\text{acc}}$  space for this object led us to prefer  $\dot{M}_{\text{acc}} \simeq 8 \times 10^{-9} M_{\odot} \text{ yr}^{-1}$  combined with  $\dot{M}_{\text{wind}} \simeq 4.8 \times 10^{-10} M_{\odot} \text{ yr}^{-1}$  ( $\sim 0.06 \dot{M}_{\text{acc}}$ ). This best value of  $\dot{M}_{\text{acc}}$  is comfortably within the allowed range discussed in Section 4 and implies a distance to RW Tri of  $D = 350 \text{ pc}$  which is reasonable. We found that a low value of the mass-loss exponent  $\alpha$  was required to achieve an acceptable match to the relative line strengths in this system. A low value of  $\alpha$  means that the density near the rotational axis of the system is small, allowing for a mean higher ionization state in this region. This was required in order to produce a sufficiently strong N V emission line, relative to C IV. Our exploration of parameters indicated that the collimation of the RW Tri wind is not very strongly constrained by the spectra. Only very low collimations (low values of  $d \lesssim 10$ ) can clearly be ruled out since they lead to clear P-Cygni profiles in C IV which are not observed. In our best model, a slightly higher collimation was adopted than in Knigge & Drew (1997), since we found that it led to a slightly better match with the data.

The spectrum obtained for this model at an inclination angle of  $75^{\circ}$  is compared to the observations in Figure 6. Details of the line profiles for the major resonance transitions of N V, Si IV, and C IV are shown in Figure 7. These are in good agreement with the observations with regard to both line width and strength. Since they form under different ionization conditions, they are present in quite different regions of the wind; see Figure 8. In particular, N V probes the highest ionization state material which exists in the innermost streamlines where the radiation temperature is high owing to the abundance of ultraviolet photons radiated by the inner regions of the disk (see Figure 9). In contrast, Si IV is confined to a relatively narrow equatorial band lying across the base of flow streamlines that rise further out in the disk. This region has lower  $T_{\text{R}}$  since it is exposed to the radiation field from the cooler outer disk regions. This, combined with the high



**Figure 6.** Comparison between RW Tri *HST* observations and our best KWD95 model.



**Figure 7.** Detailed comparison of line profiles for RW Tri and our KWD95 model during pre-eclipse (left) and mid-eclipse (right).

electron densities ( $n_e$ ) at the base of the flow, allows relatively low-ionization state material to dominate this region. C IV is present across a much wider region of the wind than either N V or Si IV, occupying most of the space between the polar regions (rich in N V) and the equatorial band of Si IV. C IV also exists throughout much of the outer wind allowing for a significantly extended region of line formation. This is a consequence of the relatively uniform distribution of  $T_{\text{R}}$  and  $n_e$  in the outer parts of the flow (see Figure 9).

In Figure 8, contours are drawn to indicate the line-forming regions. Specifically, these contour lines indicate where the last scattering events for Monte Carlo quanta which contribute to specific resonance lines took place. As one would expect from the ion distribution, C IV has a somewhat extended region of line formation, while N V and Si IV are more confined to the inner parts of the flow, being concentrated in the polar or more equatorial regions, respectively. Given these significant differences in region of line formation, it is a powerful confirmation of the wind model that the relative strengths and shapes of these main line features can be reproduced, both in and out of eclipse, by a single model in which the ionization



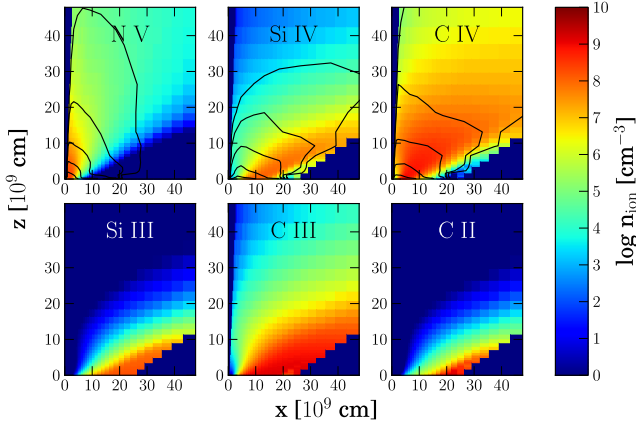


**Figure 8.** Number densities for various ions as a function of position in our wind model for RW Tri (adopting the KWD95 prescription). Only the inner portion of the wind that produces substantial scattering is shown (our computational grid extended to  $10^{13}$  cm). The black contour lines indicate the line-forming regions of the main three resonance lines (upper panels). Specifically, they are contours of the number of relevant last scattering events in a computational grid cell normalized by the cell volume. The four contours are drawn for one decade intervals in this quantity which, as expected, decreases outward.

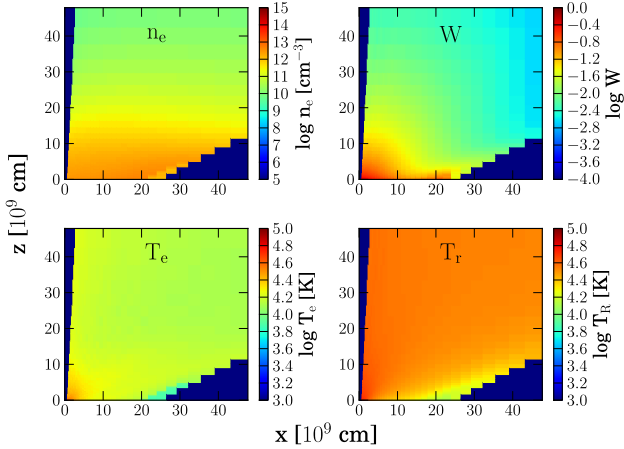


**Figure 9.** Temperature, dilution factor, and density structure of the RW Tri KWD95 model.

conditions are controlled by the radiation produced by the accretion disk.

In addition to the three major lines, several metal lines associated with lower ionization state material appear in the spectra. In the pre-eclipse spectrum, absorption by C II  $\lambda 1333$  and Si III  $\lambda \lambda 1295 - 1303$  are present in both model and observed spectra although Si III is rather too weak in the model. C III  $\lambda 1176$  also appears in both model and observation but its character is less well represented — in particular it appears as absorption in the model pre-eclipse spectrum but emission in the data. During eclipse this feature is in emission in the model but it is too weak. Taken together, this suggests that the wind model may place C III too close to the disk plane — a better match might be obtained if more of this ion existed in the extended (unclipped) wind region with less lying along our relatively high-inclination line of sight. Recombination line emission in both H I Lyman  $\alpha$   $\lambda 1215$  and He II  $\lambda 1640$

**Table 4**

Parameters for Our Best SV93 Models for RW Tri and UX UMa.

Parameter	RW Tri	UX UMa
$M_{\text{WD}}$	$0.7 M_{\odot}$	$0.47 M_{\odot}$
$M_2$	$0.6 M_{\odot}$	$0.47 M_{\odot}$
$R_{\text{WD}}$	$8.0 \times 10^8$ cm	$9.7 \times 10^8$ cm
$R_{\text{disk}}$	$2.4 \times 10^{10}$ cm	$2.9 \times 10^{10}$ cm
$i$	$75^{\circ}$	$71^{\circ}$
$D^a$	345 pc	374 pc
$\dot{M}_{\text{disk}}$	$8.0 \times 10^{-9} M_{\odot} \text{ yr}^{-1}$	$1.3 \times 10^{-8} M_{\odot} \text{ yr}^{-1}$
$T_{\text{eff}}^b$	$5.7 \times 10^4$ K	$5.1 \times 10^4$ K
$\dot{M}_{\text{wind}}$	$4.8 \times 10^{-10} M_{\odot} \text{ yr}^{-1}$	$1.0 \times 10^{-9} M_{\odot} \text{ yr}^{-1}$
$R_{\text{min}}$	$R_{\text{WD}}$	$R_{\text{WD}}$
$R_{\text{max}}$	$R_{\text{disk}}$	$R_{\text{disk}}$
$\theta_{\text{min}}$	$2^{\circ}$	$1^{\circ}$
$\theta_{\text{max}}$	$56^{\circ}$	$36^{\circ}$
$\gamma$	1	1
$\lambda$	0.6	-0.5
$f$	3	4
$R_s$	$2.0 \times 10^{11}$ cm	$4.9 \times 10^{10}$ cm
$\alpha$	2.2	1.0

**Notes.**

<sup>a</sup> Distance implied by the renormalization of the model continuum.

<sup>b</sup> Maximum effective temperature in the disk determined via Equation (1) from  $M_{\text{WD}}, R_{\text{WD}}, \dot{M}_{\text{disk}}$ .

is also predicted by the model. For He II, the recombination line strength is too small in the model but for H I Ly $\alpha$  it is significantly too strong in the pre-eclipse spectrum. This line forms rather deep in the wind models, meaning that its emission line flux is significantly affected during eclipse (compare model line strengths in Figure 6). It is therefore much more sensitive to the structure at the base of the wind than the other strong emission lines and may indicate a shortcoming of our wind models in describing those regions.

To establish the sensitivity of our conclusions about the line formation regions to the choice of how the wind is parameterized, we have also developed a wind model for RW Tri using the SV93 wind prescription. The parameters for this model are given in Table 4 and its spectrum is shown in Figure 10. These show comparably good agreement in the spectral features as found with the KWD95 model. Moreover, despite the difference in parameterization, they indicate characteristically similar geometries for the distribution of ionization states as found with the KWD95 wind prescription.

## 5.2. UX UMa

We employed a similar methodology to obtain point models for UX UMa with both the KWD95 and SV93 wind prescriptions. The parameters of these models are given in Tables 3 and 4.

Based on the fits to the continuum, we require a lower effective temperature for UX UMa meaning that the inner disk radiation is redder than in RW Tri. Thanks to this, a good match to the relative strengths of emission in N V, C IV and Si IV was obtained without having to adopt a low value for  $\alpha$  (cf. discussion of N V in RW Tri above). An important difference in the observed spectra of UX UMa compared to RW Tri, however, is the appearance of narrow absorption dips in the Si IV profile out of eclipse. We could not reproduce these dips via simple changes in either  $\dot{M}_{\text{wind}}$  or  $\alpha$ . To explain these features, it is necessary to introduce Si IV ions along the observer's line of sight which requires a more equatori-

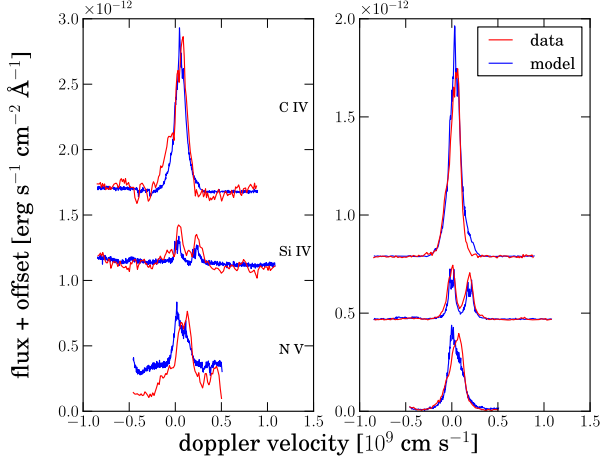


**Figure 10.** Details of line profiles for the RW Tri SV93 model during pre-eclipse (left) and mid-eclipse (right).

ally concentrated Si IV population. By exploring the velocity-law parameters, we found that this could readily be explained by a more-rapidly accelerating flow (specifically, we reduce the acceleration exponent  $\beta$ ; qualitatively similar results can be obtained with a smaller acceleration length  $R_s$ ). A more rapid acceleration reduces the density allowing Si IV to replace Si III around the base of the wind. Together with a rather high collimation of the wind, which was necessary to ensure the right width and blueshift of the Si IV absorption dips, this approach led to a reasonable match of the three main line profiles (see Figures 11 and 12). Our low value of  $\beta = 1.0$  is the most substantial difference in the wind parameters between this study and that of Knigge & Drew (1997): they favored a significantly more gradual acceleration ( $\beta = 4.5$ ) but modeled only the C IV profile and did not compute the wind ionization state in detail. Admittedly, they obtained a somewhat better fit to the C IV profile than we have (see their Figure 4); however, we find that the additional constraints on the wind properties by the complex Si IV line profile require a modification to the density structure around the base of the wind which are consistent with much more rapid acceleration. A negative consequence of the change in the density structure around the base of the wind is that this model significantly underpredicts the strengths of features associated with the lowest ionization material (e.g., C II and Si III wind features are entirely absent from the model spectra, while the recombination H I Lyman  $\alpha$  and He II  $\lambda 1640$  lines are too weak).

While the major emission lines in the model match the data well, there is a discrepancy between the slope of the model and the observed disk continuum in the pre-eclipse state. The model continuum, which reflects that of a steady-state disk, is steeper than the observed spectrum, a fact that has been known about UX UMa for some time (see, e.g. Knigge et al. 1998). One possibility is that the run of temperatures in the disk simply departs from that of a steady-state disk, an idea that was explored in detail by Linnell et al. (2008) without, in our opinion, finding an obviously better model for the disk emission. Our models would suggest that, despite the apparent mismatch in the continuum slope, the ionization conditions in the wind required to produce the correct relative strengths of the emission lines can be obtained from a standard, steady-state disk configuration: if we were to significantly alter the distribution of  $T_{\text{eff}}$  for the disk in our fiducial

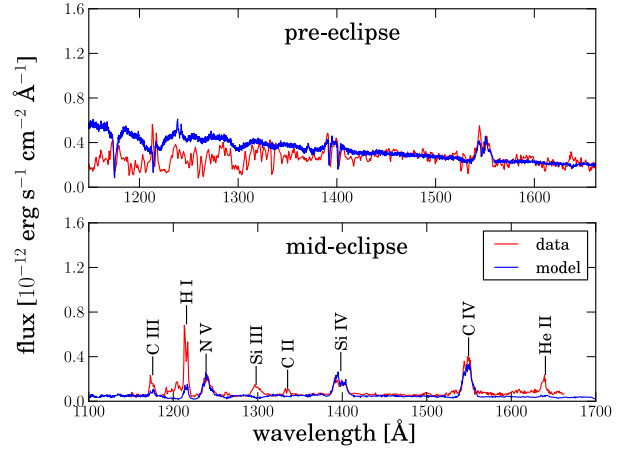


**Figure 11.** Comparison between UX UMa *HST* observations and our best KWD95 model.

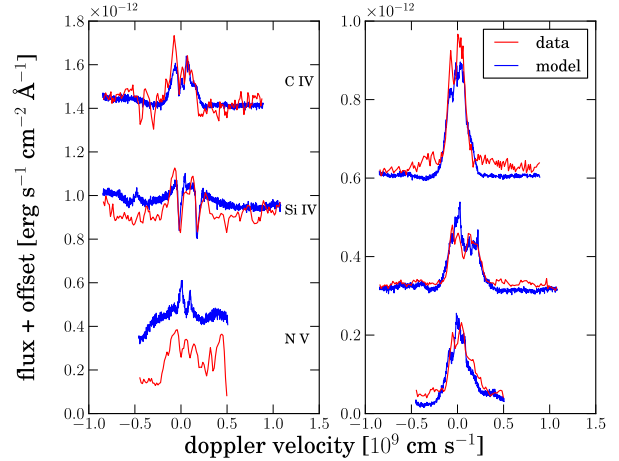


**Figure 12.** Details of line profiles for the UX UMa KWD95 model during pre-eclipse (left) and mid-eclipse (right).

model, the ionization conditions (and therefore line emission) in the wind would change. Although this might be accounted for by modifications to other wind parameters, on balance we favor an alternative possibility, namely, that the mismatch of the continuum slope is the result of occultation of the inner portion of the disk along our line of sight. This is certainly not an established fact, but UX UMa is known to exhibit pre-eclipse dips in the UV that are attributed to this effect; it is possible that portions of the disk are occulted all of the time, as is known to be the case in some SW Sex stars, including DW UMa (Knigge et al. 2004). It seems less likely to us that the disk is truncated because this would necessarily reduce the peak value of  $T_{\text{eff}}$  in the disk and therefore predict a less ionized wind.

The ionization structure of the UX UMa wind model (shown in Figure 13) is different in detail but similar in character to that in the models fit to RW Tri. The main difference is the extension of the low-ionization region near the disk which is much smaller in this model. This is a consequence of the reduction in  $\beta$  that was required to reproduce the Si IV the absorption dips.

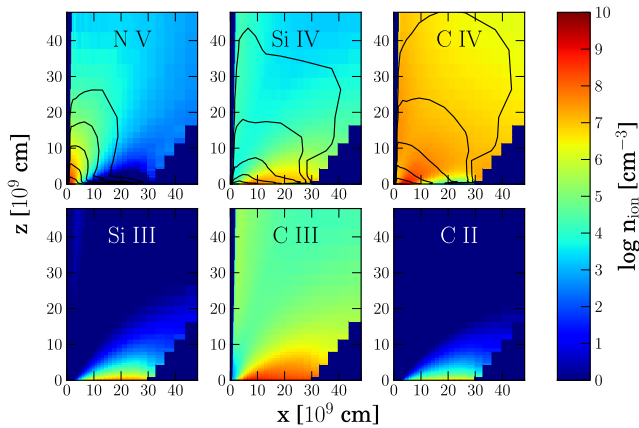


**Figure 13.** Ionization structure of the UX UMa KWD95 model. Again the line-forming regions are shown by contour lines (cf. Figure 8).

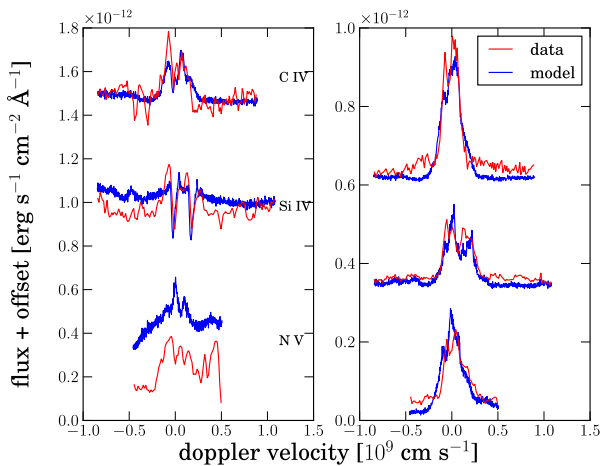


**Figure 14.** Details of line profiles for the UX UMa SV93 model during pre-eclipse (left) and mid-eclipse (right).

As for RW Tri, we were able to transform the wind parameters to the SV93 prescription and obtain a wind model which produced comparably good spectra to the best KWD95 model (Figure 14). Some minor differences appear in the profile shapes, in particular the Si IV absorption dips are slightly deeper. However, once again, the characteristic wind structure is qualitatively similar, as are the line-forming regions.

### 5.3. Similarities and Differences between the RW Tri and UX UMa wind Models

Compared to previous studies in which the ionization state of the wind has been imposed, our approach has the important advantage that the ionization conditions in the wind are treated self-consistently with the radiation field. This has directly led us to wind models with simple, physically plausible ion distributions that are characteristically similar for both the objects we have studied with both wind prescriptions. The favored picture always involves a polar concentration of N V, equatorial Si IV (and lower ions), and C IV filling most of the space between. This basic configuration was able to reproduce the observations, despite the differences in the UX UMa and RW Tri observed spectra. As one would expect, the

major line formation occurs around the regions where the relevant ions are most populated and is concentrated within the innermost few tens of WD radii.

Our studies of the two systems have favored mass loss rates which are a few percent of the accretion rates (6% and 8%). Our models suggest that these values are fairly robust — simple changes in the mass-loss rate by a factor of 2 (in either direction) leads to results which are strongly inconsistent with the observations.

The main differences between our models for RW Tri and UX UMa lie in the details of the wind structure and are connected to the differences in the KWD95 parameters  $\alpha$  (mass loss exponent) and  $\beta$  (acceleration exponent). In RW Tri, a small value of  $\alpha$  was necessary to avoid under-producing N V. The  $\alpha$ -parameter is less strongly constrained for our UX UMa point model —  $\alpha = 0.5$  agrees very well with the observations and leads to a simple wind structure but higher or lower values cannot be strongly excluded. Thus, our models do not rule out the possibility that both systems have somewhat similar radial dependence of the mass-loss rate per unit area.

On the other hand, our results relating to the wind acceleration law do seem to suggest real differences between the systems. The  $\beta$ -parameter cannot be very significantly reduced for RW Tri because this would eventually introduce strong absorption features in Si IV and C IV, neither of which is observed. (The high acceleration exponent ensures that the main Si IV region is located far above the disk, outside the line of sight.) A large value of  $\beta$  also allows for a low-ionization state region close to the disk (below the main Si IV concentration) where absorption lines seen in the pre-eclipse spectra (e.g., C II) can form. However, the UX UMa spectra also place relatively strong constraints on the wind velocity law for that system. Here, Si IV absorption dips are seen, favoring a higher ionization state closer to the disk compared to RW Tri. In our model, this increase in the ionization state was realized via a rapid acceleration (low acceleration exponent), leading to a low density. We note that this is in contrast to the study of UX UMa by Knigge & Drew (1997) in which a *high*  $\beta$ -value (i.e., *slow* acceleration) was invoked to account for absorption dips in C IV. In their approach, a constant ionization fraction was assumed meaning that deeper absorption arises from higher densities. In our case, we have to account for the fact that the density affects not only the optical depth directly but also the ionization balance. The net effect of this is that *lower* densities are needed to (see Figures 9 and 15) obtain the Si IV dips because high densities lead to too low an ionization state. Thus, we find that significantly faster acceleration is required to model the UX UMa spectra than those of RW Tri, likely pointing to a real physical difference in the manner in which the outflows of the two systems are driven.

A downside of the reduced density around the base of the flow in our UX UMa model is that the low-ionization state material is pushed very close to the disk. Thus, we lose any trace of emission or absorption signatures from very low-ionization state material in the model spectra. This suggests that a more complex wind structure (e.g., clumping) may be needed at the highest inclination to allow for the simultaneous appearance of absorption features in both relatively high ionization state lines (e.g., Si IV) and significantly less ionized material (e.g., C II). We generally found that these classes of absorption features could not be simultaneously created with the kinematic wind models we have considered.

An additional, less significant difference between the point models of UX UMa and RW Tri is the degree of wind colli-

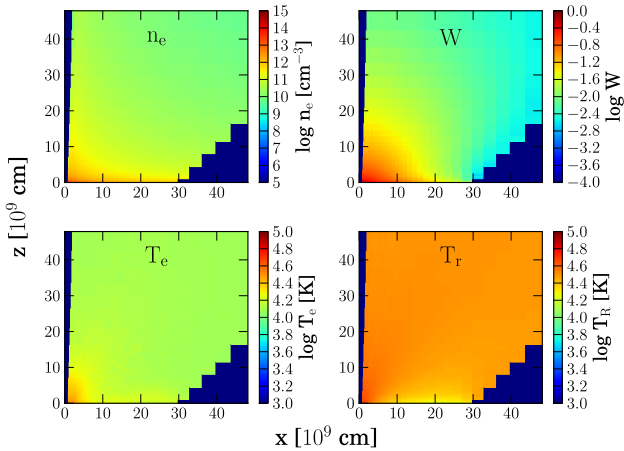


**Figure 15.** Temperature and density structure of the UX UMa KWD95 model.

mation. As noted above, there is a certain freedom for this parameter in RW Tri since the spectra are not very strongly affected by it. We can, however, exclude very low collimation since it produces P-Cygni C IV profiles which are in conflict with observation. In UX UMa, winds with very low collimation can also be excluded for the same reason. But in this system, the absorption features in Si IV give additional constraints on the collimation. A moderately high wind collimation gives the correct blueshift and width of these features, introduced by the slowly accelerating wind.

## 6. CONCLUSIONS

We have presented point models for the winds in the eclipsing CVs RW Tri and UX UMa which are able to reproduce the main characteristics of the major UV resonance lines of N V, Si IV, and C IV both in and out of eclipse. The ionization conditions in our models are primarily determined by the temperature distribution in the wind which, in turn, is determined by the effective temperature distribution of the disk. Accounting for this, we found that agreement with observation could be obtained for winds with a characteristic structure in which N V forms around the inner edge of the wind (exposed to the hottest disk radiation), while Si IV is restricted to a region around the base of the flow that extends along the equatorial edge of the flow. The equatorial location of Si IV allows for narrow absorption dips to appear in the line profile, as observed in UX UMa out of eclipse. The formation of the resonance lines of both N V and Si IV is restricted to the innermost boundaries of the wind (within a few tens of WD radii of the central object). The outer wind has ionization state intermediate between these edge zones and it is here that the strong C IV line is formed. The wind volume reasonable for this line is significantly more extended than for either of the other major resonance lines but still concentrated within  $\sim 50$  WD radii of the central object.

Although our focus has been the major resonance lines, our models include some wind regions of even lower ionization state material which are able to introduce some absorption features in the RW Tri pre-eclipse spectra due to, e.g., C II and Si III. In agreement with observations, our models also predict weak C III emission during eclipse and some recombination emission from both H I and He II. The details of these features are less well reproduced than those of the main resonance lines: in particular, H I Ly $\alpha$  is significantly overpre-

dicted by our models for RW Tri while He II is dramatically underpredicted for UX UMa. The failures are most likely associated with the manner in which our wind models describe the very base of the wind where it is densest and, perhaps, has the most complex flow geometry.

We have used two different classes of simply parameterized flow models (those due to KWD95 and SV93) and confirmed that both parameterization are able to reproduce the observations with comparable accuracy and that they lead to similar conclusions relating to the ionization and structure of the flow.

The wind structure our models suggest for both RW Tri and UX UMa are characteristically similar. Both require wind mass-loss rates which are  $\sim 6\% - 8\%$  of the accretion rate. We also found some evidence suggesting that obtaining a wind able to simultaneously account for all three of the major resonance lines may favor models in which the mass-loss per unit area of the disk is not strongly coupled to the local disk effective temperature. In particular, for RW Tri we found that adopting  $\alpha = 1$  for the KWD95 prescription (meaning that the mass loss is proportional to the local disk luminosity) significantly underpredicts the N V emission. To reproduce the observed N V line strength, we found that a much lower value of  $\alpha \sim 0.1$  was required. Qualitatively similar results were obtained from the SV93 prescription. In UX UMa, we found that the relative line strengths were less constraining on the distribution of mass loading in the wind but are also consistent with  $\alpha$ -values somewhat less than 1.0. These conclusions are likely to be affected if there are any additional sources of ionizing radiation (e.g., a hot boundary layer) that the calculations presented here do not include. Nevertheless, they may implicate mechanisms other than the radiation force alone in launching the wind since it suggests the connection between the local mass loss and luminosity in the disk may be weak.

We found some evidence for real differences in the wind properties between the two systems. In particular, our models suggest that the acceleration around the base of the flow is significantly more rapid in UX UMa than in RW Tri. This conclusion mainly stems from the presence of absorption dips in the out-of-eclipse Si IV profile of UX UMa which are absent from RW Tri. Our attempts to model these features as part of the wind argue against a universal kinematic outflow model and may suggest that there are real differences in the wind launching regions of different systems. However, further study of the structure around the base of the wind (including consideration of lower ionization state spectral features) is required to confirm this and we cannot yet rule out that the absorption dips in Si IV might have some different origin (e.g., in the rim of the accretion disk).

Overall, our results support conclusions drawn from previous theoretically motivated considerations of the structure of CV disk winds and their physical origin. In particular, as discussed by Drew & Proga (2000), the mass-loss rates predicted from simulations of radiatively driven outflows (Proga et al. 1998) are likely too small to account for the strength of observed spectral features. (Drew & Proga 2000; Proga et al. 2002). Our results strongly support this conclusion: our wind mass-loss rates are indeed significantly higher than those expected for line-driven disk wind models with a plausible value of the Eddington ratio (see Figure 1 of Drew & Proga 2000), while the disk accretion rates we have used are close to (or below) the lower limit of the regime in which radiation pressure alone might be able to drive a flow. In addition, we have concluded that the range of radii from which mass loss is launched is significantly more extended than one might ex-

pect for a radiative driven flow (i.e., the low  $\alpha$ -value which we require for RW Tri). This is in line with the discussion of Proga et al. (2002) in which they also argue that line-driven disk wind simulations do not succeed in launching fast outflows from as extended a region of the disk as suggested by observations. Thus, although the accretion and mass-loss rates implied by our models for the eclipsing nova-like variables are undoubtedly in the range where radiation forces should be dynamically important, additional physics — most plausibly magnetic phenomena — likely has a part in driving the mass loss.

This work was supported by NASA through grant HST-AR-10674.01-A from the Space Telescope Science Institute, which is operated by AURA, Inc., under NASA contract NAS5-26555. Most of the work presented here was conducted during U.M.N.'s research visit at STScI. U.M.N. thanks K.S.L. for his encouraging support and kind hospitality during that time. S.A.S. acknowledges STScI support for a collaborative visit during which part of this project was performed.

## REFERENCES

- Anders, E., & Grevesse, N. 1989, *Geochim. Cosmochim. Acta*, 53, 197  
 Baptista, R., Horne, K., Hilditch, R. W., Mason, K. O., & Drew, J. E. 1995, *ApJ*, 448, 395  
 Baptista, R., Horne, K., Wade, R. A., Hubeny, I., Long, K. S., & Rutten, R. G. M. 1998, *MNRAS*, 298, 1079  
 Blandford, R. D., & Payne, D. G. 1982, *MNRAS*, 199, 883  
 Campbell, C. G. 2010, *MNRAS*, 401, 177  
 Cannizzo, J. K. 1993, in *Accretion Disks in Compact Stellar Systems*, ed. J. C. Wheeler (Singapore: World Scientific), 6  
 Córdova, F. A., & Mason, K. O. 1982, *ApJ*, 260, 716  
 Córdova, F. A., & Mason, K. O. 1985, *ApJ*, 290, 671  
 Drew, J. E., & Proga, D. 2000, *New Astron. Rev.* 44, 21  
 Drew, J. E., & Verbunt, F. 1985, *MNRAS*, 213, 191  
 Drew, J. E., & Verbunt, F. 1988, *MNRAS*, 234, 341  
 Froning, C. S., Long, K. S., & Knigge, C. 2003, *ApJ*, 584, 433  
 Greenstein, J. L., & Oke, J. B. 1982, *ApJ*, 258, 209  
 Groot, P. J., Rutten, R. G. M., & van Paradijs, J. 2004, *A&A*, 417, 283  
 Hartley, L. E., Drew, J. E., Long, K. S., Knigge, C., & Proga, D. 2002, *MNRAS*, 332, 127  
 Hōshi, R. 1979, *Prog. Theor. Phys.*, 61, 1307  
 Herter, T., Lacasse, M. G., Wesemael, F., & Winget, D. E. 1979, *ApJS*, 39, 513  
 Howell, S. B., Nelson, L. A., & Rappaport, S. 2001, *ApJ*, 550, 897  
 Hubeny, I., & Lanz, T. 1995, *ApJ*, 439, 875  
 Kaitchuck, R. H., Schlegel, E. M., & Honeycutt, R. K. 1983, *ApJ*, 267, 239  
 Knigge, C., Araujo-Betancor, S., Gänsicke, B. T., Long, K. S., Szkody, P., Hoard, D. W., Hynes, R. I., & Dhillon, V. S. 2004, *ApJ*, 615, L129  
 Knigge, C., & Drew, J. E. 1997, *ApJ*, 486, 445  
 Knigge, C., Long, K. S., Wade, R. A., Baptista, R., Horne, K., Hubeny, I., & Rutten, R. G. M. 1998, *ApJ*, 499, 414  
 Knigge, C., Woods, J. A., & Drew, J. E. 1995, *MNRAS*, 273, 225  
 König, A., Salmeron, R., & Wardle, M. 2010, *MNRAS*, 401, 479  
 Krautter, J., Vogt, N., Klare, G., Wolf, B., Duerbeck, H. W., Rahe, J., & Wargau, W. 1981, *A&A*, 102, 337  
 La Dous, C. 1991, *A&A*, 252, 100  
 Linnell, A. P., Godon, P., Hubeny, I., Sion, E. M., & Szkody, P. 2008, *ApJ*, 688, 568  
 Long, K. S., & Knigge, C. 2002, *ApJ*, 579, 725  
 Mason, K. O., Drew, J. E., Córdova, F. A., Horne, K., Hilditch, R., Knigge, C., Lanz, T., & Meylan, T. 1995, *MNRAS*, 274, 271  
 Mason, K. O., Drew, J. E., & Knigge, C. 1997, *MNRAS*, 290, L23  
 Mauche, C. W., & Raymond, J. C. 1987, *ApJ*, 323, 690  
 Mazzali, P. A., & Lucy, L. B. 1993, *A&A*, 279, 447  
 McArthur, B. E., et al. 1999, *ApJ*, 520, L59  
 Mineshige, S. & Osaki, Y. 1983, *PASJ*, 35, 377  
 Pringle, J. E. 1989, *MNRAS*, 236, 107  
 Proga, D., Kallman, T. R., Drew, J. E., & Hartley, L. E. 2002, *ApJ*, 572, 382  
 Proga, D., Stone, J. M., & Drew, J. E. 1998, *MNRAS*, 295, 595  
 Rutten, R. G. M., van Paradijs, J., & Tinbergen, J. 1992, *A&A*, 260, 213  
 Schlegel, E. M., Honeycutt, R. K., & Kaitchuck, R. H. 1983, *ApJS*, 53, 397  
 Schreiber, M. R., Gänsicke, B. T. 2002, *A&A*, 382, 124  
 Shlosman, I., & Vitello, P. 1993, *ApJ*, 409, 372  
 Sim, S. A., Drew, J. E., & Long, K. S. 2005, *MNRAS*, 363, 615  
 Vande Putte, D., Smith, R. C., Hawkins, N. A., & Martin, J. S. 2003, *MNRAS*, 342, 151  
 Verbunt, F. 1987, *A&AS*, 71, 339  
 Vitello, P., & Shlosman, I. 1993, *ApJ*, 410, 815  
 Wade, R. A. 1984, *MNRAS*, 208, 381  
 Woods, J. A. 1991, PhD thesis, Univ. Oxford,  
<http://adsabs.harvard.edu/abs/1991PhDT.....242W>